Analysis of the Deformation Behavior in Tension and Tension-Creep of Ti-3Al-2.5V (wt pct) at 296 K and 728 K (23 °C and 455 °C) Using *In Situ* SEM Experiments

HONGMEI LI, CARL J. BOEHLERT, THOMAS R. BIELER, and MARTIN A. CRIMP

The deformation behavior of a Ti-3Al-2.5V (wt pct) near-α alloy was investigated during *in situ* deformation inside a scanning electron microscopy (SEM). Two plates with distinct textures were examined. Tensile experiments were performed at 296 K and 728 K (455 °C) (~0.4T_m), while a tensile-creep experiment was performed at 728 K (455 °C) and 180 MPa (σ/σ_{ys} = 0.72). The active deformation systems were identified in the α phase using electron backscattered diffraction based slip-trace analysis and SEM images of the surface. Prismatic slip deformation was the dominant slip mode observed for all the experiments in both plates, which was supported by a critical resolved shear stress (CRSS) ratio analysis. However, due to the texture of plate 1, which strongly favored the activation of prismatic slip, the percentages of prismatic slip activity for specimens from plate 1 tested at 296 K and 728 K (23 °C and 455 °C) were higher than the specimens from plate 2 under the same testing conditions. T1 twinning was an active deformation mode at both 296 K and 728 K (23 °C and 455 °C), but the extent of twinning activity decreased with increased temperature. T1 twinning was more frequently observed in specimens from plate 2, which exhibited a higher fraction of twinning systems favoring activation at both 296 K and 728 K (23 °C and 455 °C). The tension-creep experiment revealed less slip and more grain boundary sliding than in the higher strain rate tensile experiments. Using a previously demonstrated bootstrapping statistical analysis methodology, the relative CRSS ratios of prismatic, pyramidal $\langle a \rangle$, pyramidal $\langle c+a \rangle$, and T1 twinning deformation systems compared with basal slip were calculated and discussed in light of similar measurements made on CP Ti and Ti-5Al-2.5Sn (wt pct).

DOI: 10.1007/s11661-014-2576-7

I. INTRODUCTION

TITANIUM (Ti) and Ti alloys are commercial materials used in structural applications in which low density and corrosion resistance are important, including armor, portable electronic devices, biomedical devices, automobiles, and aerospace components. A thorough understanding of the deformation mechanisms is required for the development of Ti alloys with enhanced mechanical performance and predictable lifetimes. When Al is added to Ti, significant strengthening of the α phase results and a desirable balance of strength, toughness, elongation-to-failure, and fatigue and creep resistance can be obtained. Additions of β-phase stabilizer elements, such as V, also contribute to improve properties due to the resulting two-phase α + β microstructure. A large body of work exists on the deformation mechanisms for the most commercially used Ti alloy, Ti-6Al-4V (wt pct)*.[1–8] However, understanding the details of deformation behavior of this alloy can be challenging due to the wide variety of α + β microstructures that can arise from different thermomechanical processing (TMP) histories.[9,10] A simpler task is to understand the deformation of single-phase α or near-α microstructures. For this reason, a number of previous studies have examined the details of the deformation mechanisms of CP Ti.[1,11–16] These studies have found that prismatic slip dominates, with additional activation of basal slip and a number of different twinning modes. Al additions have been shown to result in the suppression of twinning, as has been reported for monotonic deformation of Ti-5Al single crystals,[17] Ti-6Al single crystals,[16] and Ti-6Al-4V alloy.[1,5] For a near-α Ti-5Al-2.5Sn alloy microstructure having about 1 vol pct β phase, significantly reduced twinning activity, increased relative slip resistance to prismatic slip, and enhanced basal slip have been reported.[12,18] However, extensive twinning activity has been observed in textured polycrystalline Ti-6Al-4V alloys deformed in compression[4,19] and simple shear.[20] Thus, the deformation

*Henceforth, all alloy compositions are given in weight percent.

HONGMEI LI, formerly Ph.D. Student with Michigan State University, 428 South Shaw Lane, East Lansing, MI 48824, is now Employee with Intel, Portland, OR. CARL J. BOEHLERT, Associate Professor, THOMAS R. BIELER and MARTIN A. CRIMP, Professors, are with the Department of Chemical Engineering and Materials Science, Michigan State University. Contact e-mail: Boehlert@egr.msu.edu

Manuscript submitted November 12, 2013.
Article published online October 4, 2014

mechanisms of Ti-6Al-4V are complicated, and it appears that variations in the deformation mode distributions may arise due to differences in composition, texture, microstructure, and testing mode. This suggests that evaluating an alloy of intermediate composition, such as Ti-3Al-2.5V, which contains an intermediate volume fraction of the β phase, may be insightful for understanding the differences in the deformation mode distributions that are caused by composition, microstructure, and texture.

Ti-3Al-2.5V, known as ''half Ti-6Al-4V'', is a near-α alloy that exhibits a small amount of β phase. Like Ti-6Al-4V, Ti-3Al-2.5V exhibits a higher strength-to-weight ratio than unalloyed Ti,[21] but it exhibits a lower yield strength and better cold formability, higher elongation-to-failure, and more corrosion resistance than Ti-6Al-4V.[21] It is frequently used in the aerospace industry as fasteners and seamless tubing for aircraft hydraulic systems and for compressor blades for jet engines.[9,22] Nevertheless, the deformation evolution and mechanisms of Ti-3Al-2.5V have not been well documented as a function of temperature and testing condition. Most of the creep studies of this alloy have utilized *ex situ* characterization involving testing using conventional lever-arm load frames followed by scanning electron microscope (SEM) and transmission electron microscope (TEM) post-test characterization.[23–25] Using such conventional testing methods, the deformation and failure mechanisms may be inferred from the observation of the microstructural changes caused by mechanical testing, as well as from the shape of the stress–strain–time curves. Limitations of *ex situ* experiments include not knowing the order of activation of the different slip and twinning deformation modes nor the stress or strain at which they occur during the experiment. These disadvantages can be overcome by utilizing *in situ* testing methods, which allow for the observation of the evolution of the microstructure in real time and therefore facilitate the study of the kinematics of the deformation and failure mechanisms.[12,18,26–28] A limitation of *in situ* SEM testing is that only the surface behavior, which is likely to have somewhat different stress constraints than the bulk microstructure, is characterized.

The current work investigates the fundamental deformation mechanisms of Ti-3Al-2.5 V during tensile and tensile-creep tests using an *in situ* SEM-based testing methodology. There is not much literature focusing on the deformation mechanisms and the deformation behavior in Ti-3Al-2.5V, and there is no work that has quantitatively measured the distribution of the deformation modes in Ti-3Al-2.5V. Understanding the relative activity of these different deformation modes in different alloys is critical to the accurate modeling of the deformation behavior of such alloys and critical to making deformation/lifetime predictions under service conditions. This study provides two new aspects to the literature on Ti-3Al-2.5V: a quantitative view of the distribution of the deformation modes and an estimation of the critical resolved shear stress (CRSS) values using a methodology based on the distribution of the deformation modes.

II. EXPERIMENTAL METHODS

The Ti-3Al-2.5V alloy examined in this study was provided by Pratt & Whitney, Rocketdyne. Two 1.5-mm-thick plates with significantly different textures were examined in this work (*i.e.*, plate 1 and plate 2). The bulk chemical compositions of these two plates were similar, as measured using optical emission spectroscopy (OES) by NSL Analytical Services Inc. (Cleveland, OH), see Table I. Flat dog-bone-shaped specimens, see 2Figure 1, were electrodischarge machined from the two plates with the tensile axes parallel to the rolling direction. The specimens were mechanically polished and finished with a mixture of five parts colloidal silica (0.06 μm) and one part hydrogen peroxide. A field emission gun Camscan MIRA3 SEM (Cambridge, UK), equipped with an EDAX-TSL (Mahwah, NJ, USA) electron backscattered diffraction (EBSD) system, was used to obtain orientation maps using a 0.75 μm step size for the undeformed specimens. Both 0.75 and 0.08 μm step sizes were used for deformed specimens. Phase volume percentages were determined using ImageJ image analysis software on backscattered electron (BSE) SEM photomicrographs. The equiaxed grain sizes were measured using the line-intercept method.[29]

One specimen from each plate was tensile deformed at 296 K and 728 K (23 °C and 455 °C). The four tensile

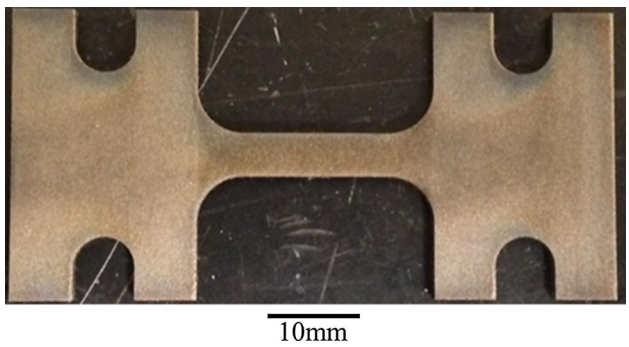

Fig. 1—A photo of an *in situ* test specimen representative of those used in the tensile and tensile-creep experiments.

Table I. Chemical Composition of Ti-3Al-2.5V (Weight Percent)

	Al	V	Fe	O	C	N	H	Ti
Plate 1	2.86	2.63	0.18	0.085	0.0115	0.0033	0.0017	balance
Plate 2	2.89	2.49	0.18	0.092	0.0097	0.0040	0.0024	balance

tests were performed inside the MIRA3 SEM at an approximate strain rate of 10^{-3} s^{-1}, based on the cross-head displacement rate. The tensile tests were periodically paused to acquire high-quality secondary electron (SE) SEM images of the surface deformation evolution. Local strains were determined by measuring the relative displacements of obvious features, such as triple points and polishing defects, on *in situ* collected images acquired before, during, and after deformation, and these values are provided for each of the SEM images of the deformed samples. The details of the *in situ* experimental setup and configuration are documented in Reference 18. The tensile data are reported in the form of engineering stress *vs* displacement plots because using the *in situ* testing technique, we do not measure the instantaneous cross-sectional area of the specimens, but we focus on the surface deformation and are able to measure the local displacements along the tensile direction. Thus, the stress data are provided in terms of engineering stress instead of true stress, and the strain data are presented in terms of engineering strain instead of true strain.

An additional specimen from plate 1 was tested under tensile-creep conditions of 728 K (455 °C) and 180 MPa, which represents approximately 0.72 of the yield stress at this temperature. SE images were acquired during the experiment without pausing the test. Strains were similarly measured as described above.

The Schmid factor for each slip/twinning system was calculated based on the deformed EBSD-measured orientation assuming a global stress state of uniaxial tension. A detailed description of the slip/twinning trace technique can be found in Reference 18. Because there are three different slip directions on the basal (three $\langle a \rangle$) and pyramidal (one $\langle a \rangle$ and two $\langle c+a \rangle$) planes, the slip direction cannot be unambiguously determined by slip-trace analysis, so the slip system with the highest Schmid factor was assumed to be the active slip system when basal or pyramidal plane traces were observed. It should be noted that when Burgers vectors are parallel to the sample surface, slip lines become difficult to detect. Furthermore, if the magnitude of slip on a particular system was small, the identification of the associated slip traces can also be difficult. Therefore, the activation of some of the deformation systems may not have been detected.

III. RESULTS

A. *Microstructure and Texture*

The two Ti-3Al-2.5V plates exhibited similar microstructures. Figure 2 shows a typical BSE image of the two-phase $\alpha + \beta$ microstructure of the as-received Ti-3Al-2.5V alloy. The bright phase in Figure 1 is the β phase, which comprised 6.1 ± 1.1 pct of the total volume as measured through image analysis and is distributed along the α/α grain boundaries and at triple points. Contrast variations observed in the darker α grains are a consequence of the electron channeling effect coupled with the variation in α grain orientation.

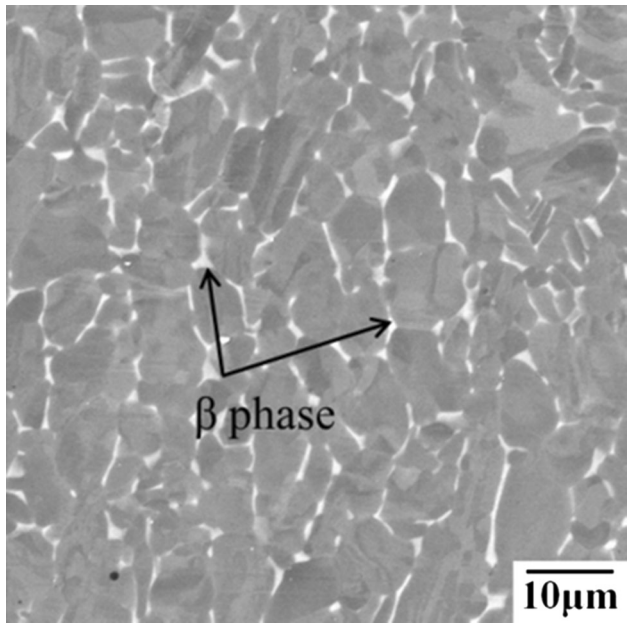

Fig. 2—BSE SEM photomicrographs of the as-received Ti-3Al-2.5V alloy, where the β phase (light color) decorated the grain boundaries or triple points.

Using a method described by Glavicic *et al.*,[30,31] it was determined that sometimes several α grains shared a common β variant and that the β orientations varied in different places. The average α grain size was 5.1 ± 0.8 μm in both plates. This analysis suggests that the size of the prior β grains was ~10 to 20 μm and that the microstructural patch shown in Figure 2 originated from β grains with a variety of grain orientations. It was ruled out that the microstructure could have been transformed from one parent β orientation.

Figure 3 shows the $\{0001\}$ and $\{10\bar{1}0\}$ pole figures, obtained using EBSD, of the five specimens prior to testing. The pole figures were collected from areas of approximately 250×200 μm^2 for each specimen and show that the materials exhibited a moderate texture (~4 to 6 times random). Pole figures (a), (c), and (e) are from plate 1 and show most grains had c-axes orientated within 30 deg of the transverse direction, so the tensile tests resulted in high Schmid factors for prismatic slip in many grains. Due to the more random nature of the texture of plate 2 shown in pole figures (b) and (d), the Schmid factors were not heavily biased for any particular deformation system.

B. *In situ Tensile Deformation*

The engineering stress *vs* displacement curves for the 296 K and 728 K (23 °C and 455 °C) tensile tests of plate 1 and plate 2 are illustrated in Figure 4. None of the specimens were taken to failure, but a minimum local strain of ~6.5 pct was achieved. The stress-displacement curve of plate 1 deformed at 296 K (23 °C) was similar to that of plate 2 deformed at 296 K (23 °C), except that the yield stress was slightly lower. The stress-displacement curves collected at 728 K

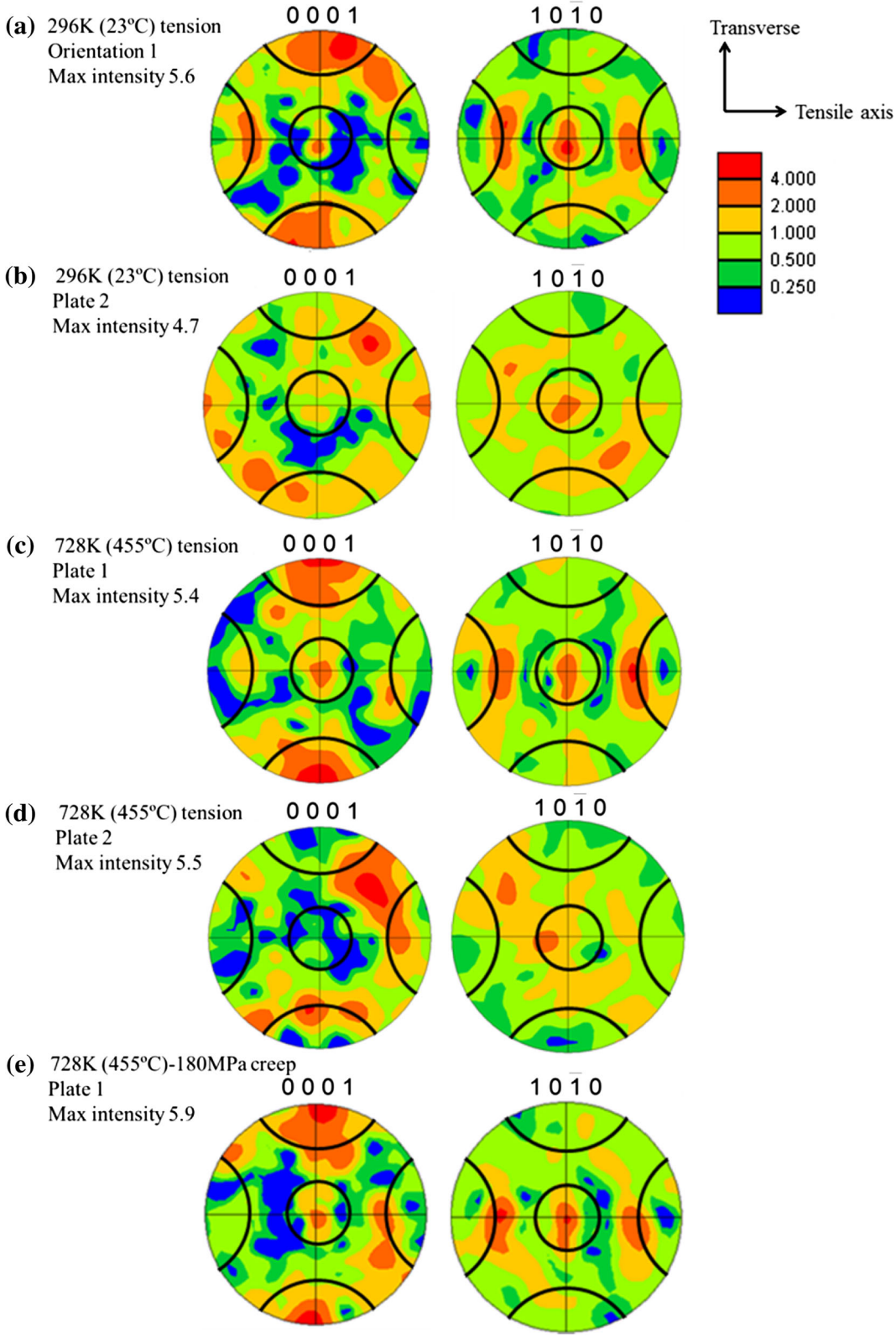

Fig. 3—The {0001} and {10$\bar{1}$0} pole figures with 30 deg cones along the major axis for (*a*) plate 1 tensile tested at 296 K (23 °C), (*b*) plate 2 tensile tested at 296 K (23 °C), (*c*) plate 1 tensile tested at 728 K (455 °C), (*d*) plate 2 tensile tested at 728 K (455 °C), and (*e*) plate 1 tensile-creep tested at 728 K (455 °C) and 180 MPa. The loading direction was horizontal. This EBSD data was acquired prior to testing.

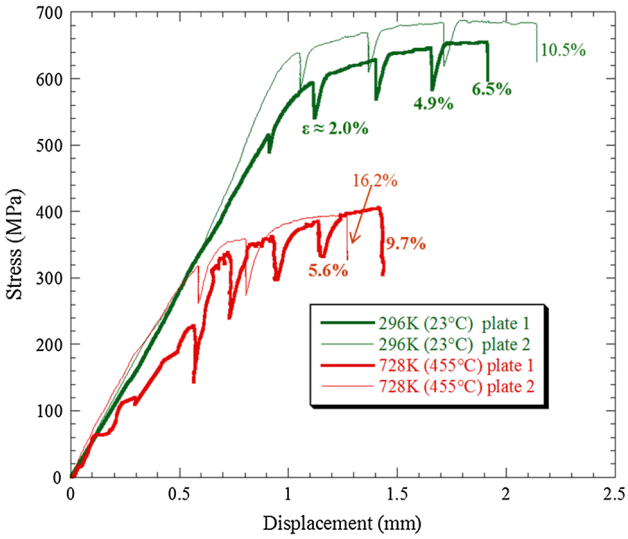

Fig. 4—Stress *vs* displacement plots for Ti-3Al-2.5V samples tensile tested at 296 K and 728 K (23 °C and 455 °C). The load drops indicate that stress relaxation occurred when the tests were interrupted for imaging. The displacement values included displacements in both the gage section and the grip regions. The local strains values measured from the SEM images are indicated on the plot for each specimen.

(455 °C) show that the yield stresses of plate 1 and plate 2 exhibited no significant difference. Overall, from 296 K to 728 K (23 °C to 455 °C), the YS of Ti-3Al-2.5V decreased from ~560 MPa for plate 1 and ~600 MPa for plate 2 to ~250 MPa for both plates.

1. *Plate 1 tensile tested at 296 K (23 °C)*

Sequential SE SEM images of the same area taken at different strains during the 296K (23 °C) tensile experiment of plate 1 are shown in Figure 5. No slip traces were observed within the elastic limit even for stresses as high as 510 MPa. Slip traces were first observed in some α grains at 595 MPa (~2 pct strain), which was just after global yielding (~560 MPa). In Figure 5(b), the slip traces were difficult to see and one grain was magnified to show an example of the slip traces observed in this grain. At ~2 pct strain, most of the traces were identified to be prismatic slip with Schmid factors greater than 0.4 (highlighted by red lines in Figure 5(b)). Basal slip was not observed in this microstructural patch. Usually, only a single slip system was identified in each grain. After ~6.5 pct strain, about 15 pct of the grains exhibited slip traces and significant surface relief was observed at the α/β phase boundaries.

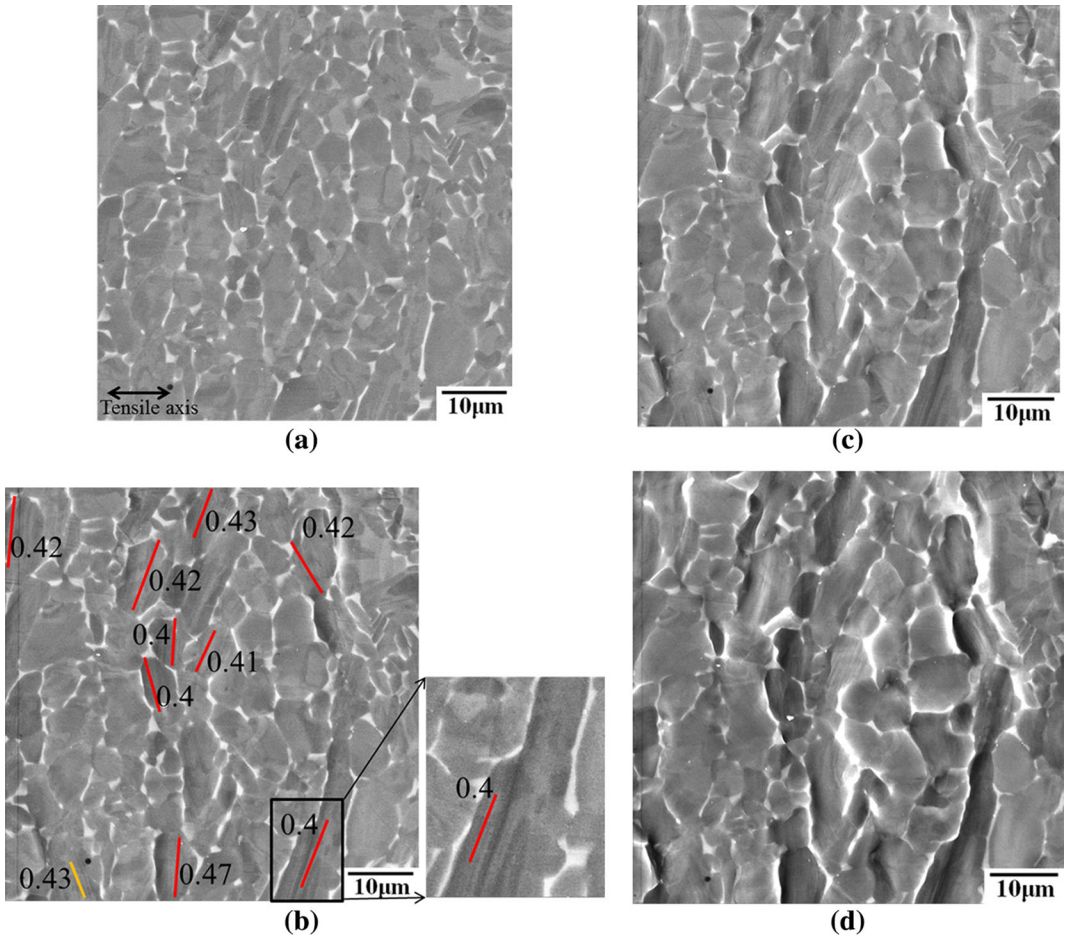

Fig. 5—Sequential SE SEM images for Ti-3Al-2.5V plate 1 tensile tested at 296 K (23 °C): (*a*) undeformed, (*b*) 595 MPa (~2.0 pct strain, when slip bands were first observed), the color-coded planes traces for prismatic slip (red) and pyramidal $\langle c+a \rangle$ (orange) are labeled along with their Schmid factors and one grain outlined in black was magnified (see insert) to show an example of observations of slip traces, (*c*) 646 MPa (~4.9 pct strain), and (*d*) 656 MPa (~6.5 pct strain) were acquired. The loading direction was horizontal.

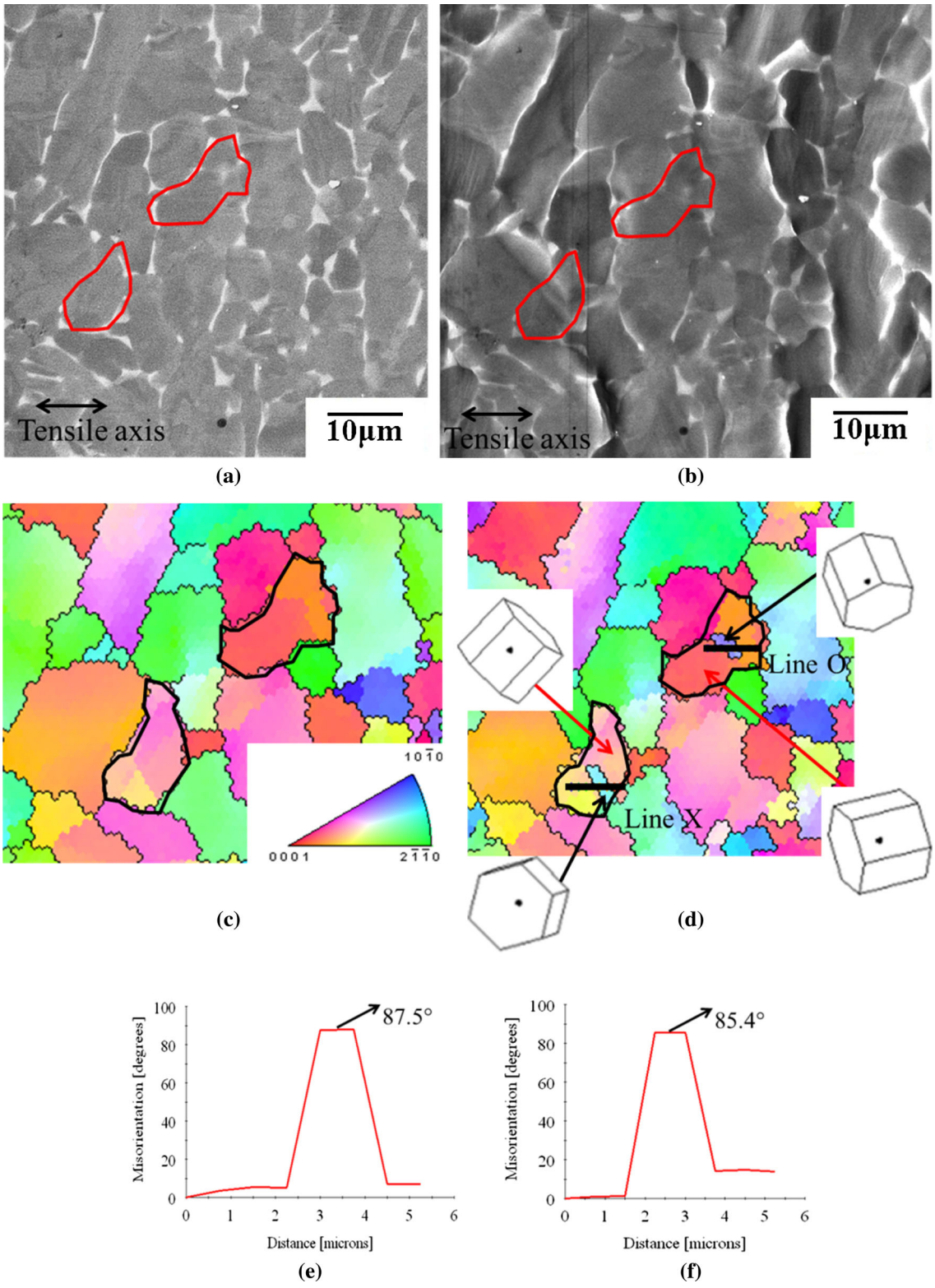

Fig. 6—(*a*) Undeformed and (*b*) deformed microstructure patch which exhibited deformation twinning during the 296 K (23 °C) tension test of plate 1 after ~6.5 pct strain with the corresponding EBSD orientation map (*c*) before and (*d*) after deformation. The grains highlighted in red in (a) and (b) indicated the parent grains where the twins formed. The red arrows in (d) point to the parent orientation and the black arrows indicate the newly formed twin orientations. Two misorientation profiles across the parent and twin grains are plotted in (*e*) and (*f*), corresponding to lines X and O in (d).

Twinning was an active deformation mode in the plate 1 tested at 296 K (23 °C). Due to the fine α-phase grain size and low contrast in these grains, it was often hard to distinguish between the twin and the parent grain[4] in BSE images, see Figure 5. Therefore, twins were found by comparing EBSD maps collected before and after deformation, as twinned regions show large orientation changes in grains, as illustrated in Figure 6. The particular twinning systems were characterized by determining the misorientation between the parent and the twin. A ~85 deg misorientation indicates a T1 twin, and the rotation axis determines which of the six $\langle 2\bar{1}\bar{1}0\rangle$ T1 twinning systems was active,[32,33] as illustrated in Figure 6. In Figure 5, two parent grains are outlined in red in Figures 5(a) and (b) and black in Figures 5(c) and (d). The misorientation across the parent and twin grains in the misorientation profiles in Figures 6(e) and (f) showed that there was ~85 deg misorientation between the twins and the corresponding parent grains. Note that only T1 twinning was observed for the Ti-3Al-2.5V alloy. Comparison of the EBSD maps before and after straining revealed that no grains had completely reoriented due to twinning.

The slip-trace technique was used to identify activation of 128 active deformation systems in 125 α grains. Of the 128 active slip systems, 102 of them (80 pct) were identified to be for prismatic slip. There were some instances of T1 twinning (12/128 ≈ 10 pct), basal slip (2/128 ≈ 2 pct), pyramidal $\langle a\rangle$ slip (9/128 ≈ 7 pct), and pyramidal $\langle c+a\rangle$ slip (2/128 ≈ 2 pct). A histogram shown in Figure 7 illustrates the basal, prismatic, pyramidal $\langle a\rangle$, pyramidal $\langle c+a\rangle$ slip, and T1 twinning distribution with respect to the global Schmid factors after ~6.5 pct strain. The activation of the different deformation systems was correlated with high Schmid factors as 76 pct of the active deformation systems exhibited global Schmid factors greater than 0.4.

2. *Plate 2 tensile tested at 296 K (23 °C)*

The deformed microstructure of plate 2 tensile tested at 296 K (23 °C) after ~10.5 pct strain is shown in Figure 8. After ~10.5 pct strain, about 25 pct of grains exhibited slip traces and a total of 124 active deformation systems were identified in 117 α grains, shown in Figure 9. More than 69 pct of the observed deformation systems activated had Schmid factors greater than 0.4. Similar to plate 1 tested at 296 K (23 °C), prismatic slip was the most active deformation system, and it comprised 48 pct of the total slip systems observed. However, this percentage is much smaller than that for plate 1 tested at 296 K (23 °C), where prismatic slip comprised 80 pct of the total observed deformation systems. Correspondingly, the percentages of basal, pyramidal $\langle a\rangle$, pyramidal $\langle c+a\rangle$, and T1 twins increased from 2, 7, 2, and 10 pct, respectively, for the specimen from plate 1 tested at 296 K (23 °C) to 8, 15, 6, and 23 pct, respectively, for the specimen from plate 2 tested at 296 K (23 °C). The observation of extensive twinning

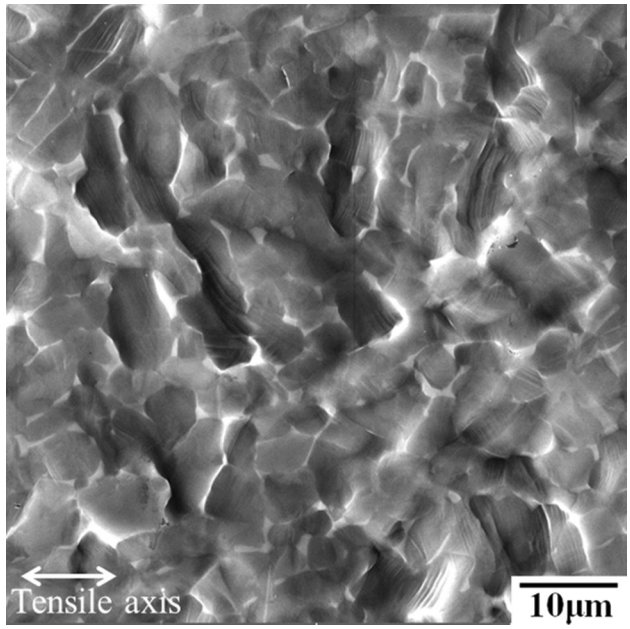

Fig. 8—BSE SEM image showing a microstructural patch of the plate 2 tensile deformed at 296 K (23 °C) after ~10.5 pct strain.

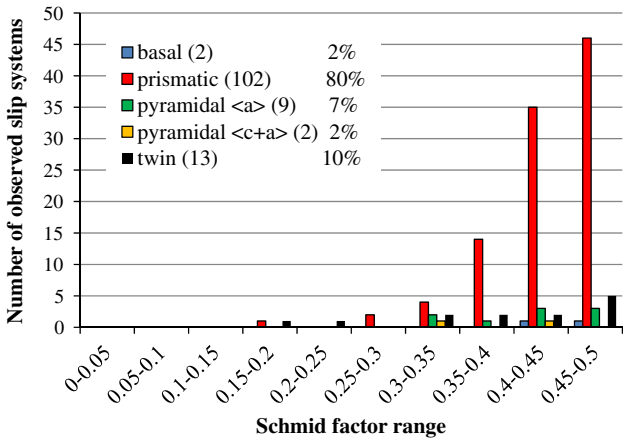

Fig. 7—Histogram of the number of observed deformation systems *vs* the global Schmid factor range taken for the plate 1 tensile tested at 296 K (23 °C) after ~6.5 pct strain.

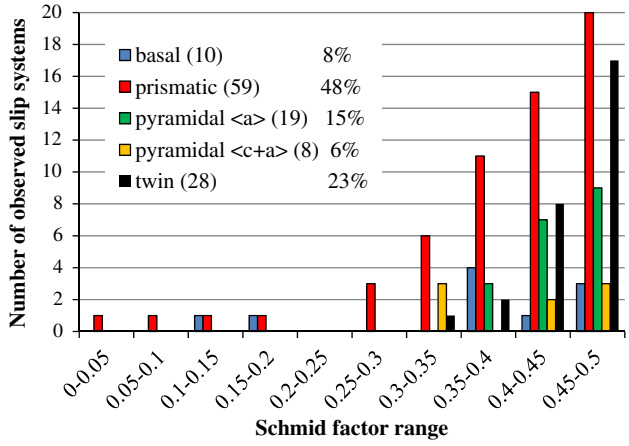

Fig. 9—Histogram of the number of observed deformation systems *vs* the global Schmid factor range taken for the plate 2 tensile tested at 296 K (23 °C) after ~10.5 pct strain.

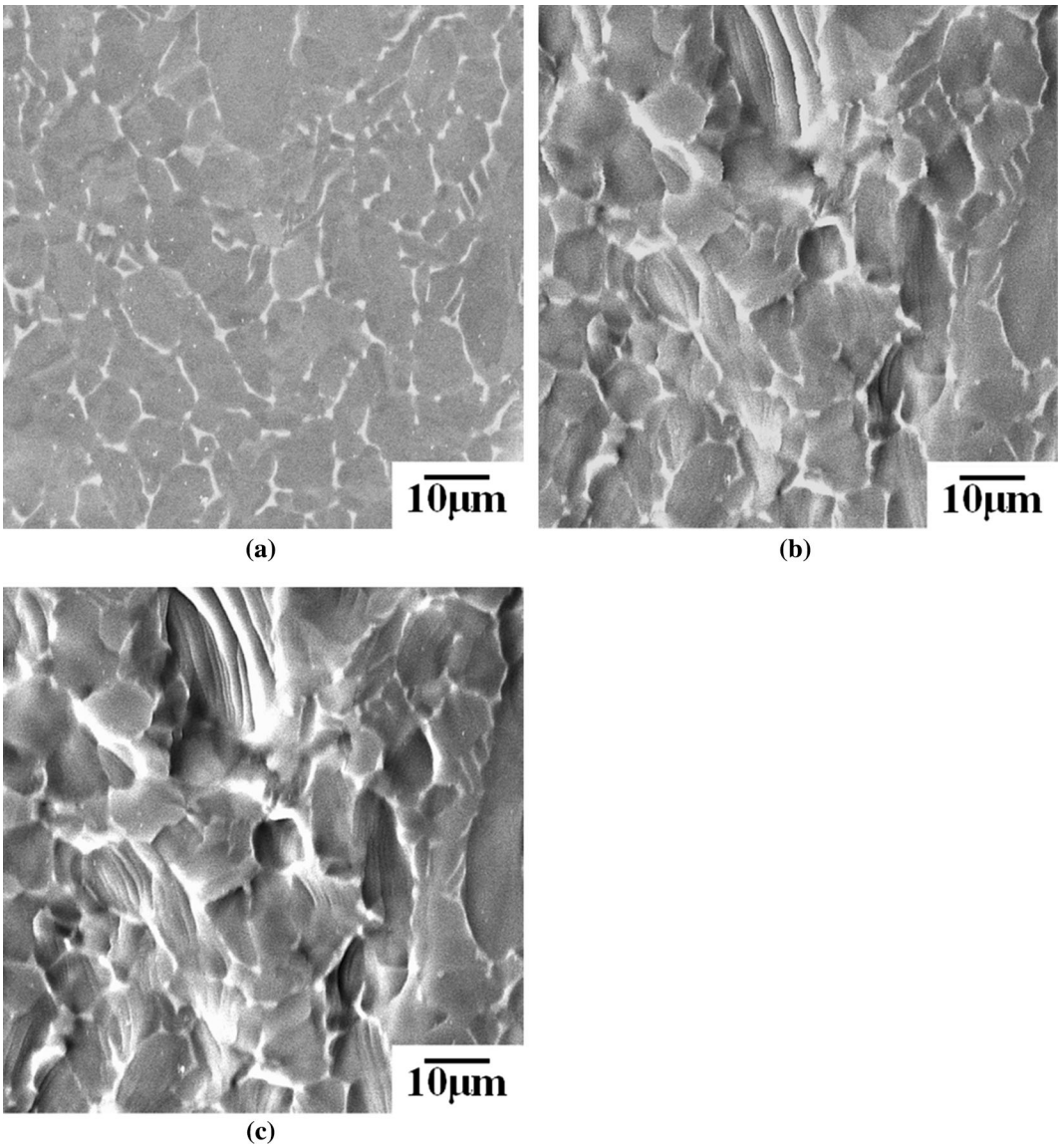

Fig. 10—SE SEM photomicrographs acquired during the 728 K (455 °C) tensile experiment of plate 1: (*a*) before loading; (*b*) ~5.6 pct strain; (*c*) ~9.7 pct strain. The loading direction was horizontal.

suggests that this is a significant deformation system in Ti-3Al-2.5V at 296 K (23 °C).

3. *Plate 1 tensile tested at 728K (455 °C)*

Sequential SE SEM images taken of plate 1 tensile deformed at 728 K (455 °C) to 0, ~5.6, and ~9.7 pct strain are shown in Figure 10. After ~9.7 pct strain, about 45 pct of grains exhibited slip traces. Grain boundary relief, suggesting sliding, was observed during the deformation. Compared with the plate 1 deformed at 296 K (23 °C), (compare Figures 5(d) and 10(b), both at ~6 pct strain), the extent of the surface relief was much more dramatic at 728 K (455 °C), which is likely to result from an increase in the grain boundary mobility assisted by the elevated temperature.

The distributions of the active deformation systems, determined for 112 slip traces in 105 α grains, are shown in Figure 11. Among the 112 active deformation systems analyzed, 7 were basal (6 pct), 75 were prismatic (67 pct), 19 were pyramidal $\langle a \rangle$ (17 pct), 7 were pyramidal $\langle c+a \rangle$ (6 pct), and 4 were T1 twins (4 pct). About 76 pct of the active deformation systems exhibited Schmid factors greater than 0.4. While the majority of deformation systems are again prismatic, the distributions of the other deformation systems have changed relative to plate 1 tested at 296 K (23 °C). For example, there were fewer twins observed at 728 K (455 °C) and these T1 twins were only observed in grains with Schmid factors greater than 0.4.

4. *Plate 2 tensile tested at 728 K (455 °C)*

An image of the microstructural patch studied in plate 2 tensile deformed at 728 K (455 °C) to ~16.2 pct strain is shown in Figure 12. Similar to plate 1 tested at 728 K (455 °C), both slip lines and a large amount of surface relief were observed. About ~54 pct of the grains

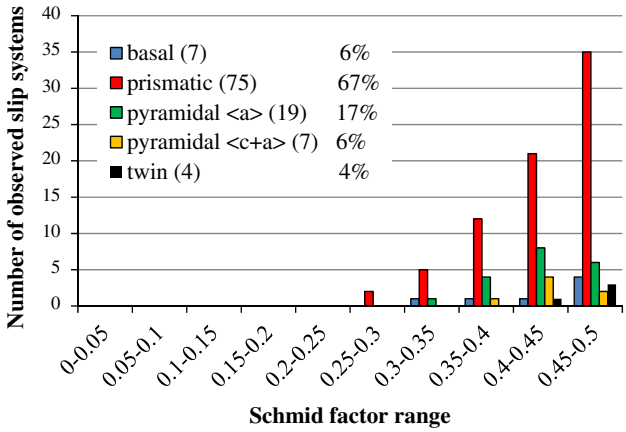

Fig. 11—Histogram of the number of observed deformation systems *vs* the global Schmid factor range taken for the plate 1 tensile tested at 728 K (455 °C) after ~9.7 pct strain.

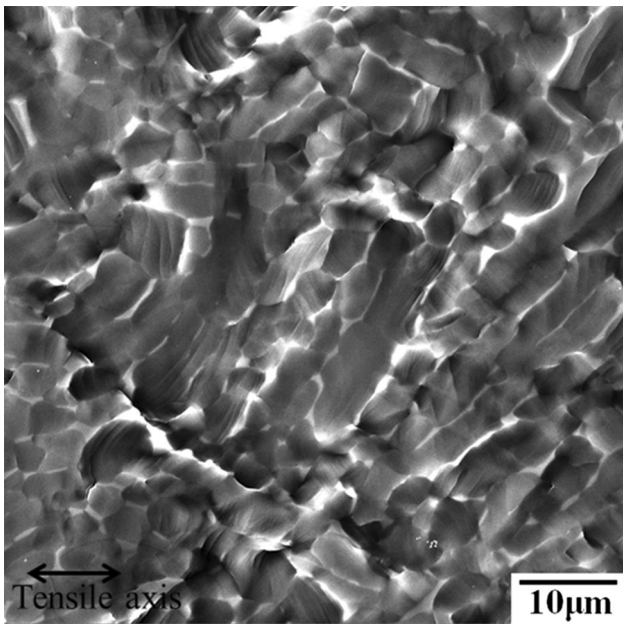

Fig. 12—BSE SEM image showing a microstructural patch of the plate 2 tensile deformed at 728 K (455 °C) after ~16.2 pct strain.

exhibited slip traces. The active deformation modes were determined for the 133 observed deformation systems in 130 α grains: 19 were basal (14 pct), 65 were prismatic (49 pct), 33 were pyramidal $\langle a \rangle$ (25 pct), 8 were pyramidal $\langle c+a \rangle$ (6 pct), and 8 were T1 twins (8 pct), as shown in the histogram in Figure 13. Despite the much weaker texture, prismatic slip was still the dominant deformation system for this plate. However, prismatic slip accounted for a lower percentage of the total observed deformation systems in plate 2 (49 pct) compared with plate 1 (67 pct). The observed active deformation systems were again dominated by systems with Schmid factors greater than 0.4 (75 pct) and no slip systems with global Schmid factors below 0.1 were observed. T1 twinning was the only twinning mode observed and the Schmid factors associated with these twins were greater than 0.35.

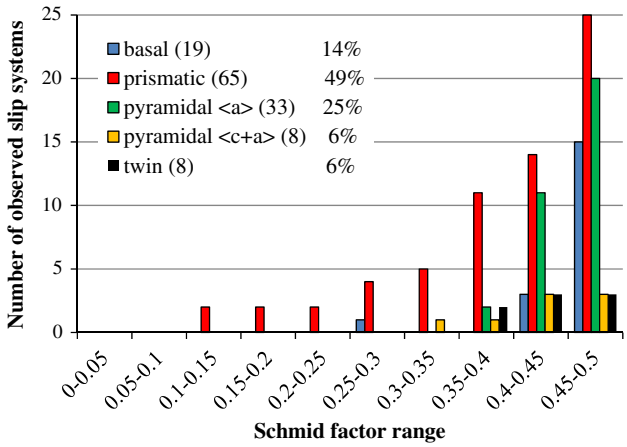

Fig. 13—Histogram of the number of observed deformation systems *vs* the global Schmid factor range taken for the plate 2 tensile tested at 728 K (455 °C) after ~16.2 pct strain.

C. *Plate 1 Creep Tested at 728 K (455 °C) and 180 MPa*

Sequential SE SEM images taken from the 728 K (455 °C)-180 MPa (~0.72 yield stress) tensile-creep experiment are shown in Figure 14. Grain boundary ledges were distinguishable after ~1.4 pct strain. Almost all the grain boundaries developed some degree of ledges after ~11.7 pct strain. Only about 3 pct of the total number of grains exhibited slip traces, indicating that dislocation slip was not the dominant deformation mechanism. Only one deformation system was observed in any given grain, with a total of 23 grains displaying identifiable slip traces. These observations are summarized in Figure 15, which show the deformation system distribution with respect to the global Schmid factors. In Figure 15, no slip systems with global Schmid factors below 0.35 were observed, indicating that the global Schmid factor is an effective parameter associated with the slip system activation under creep conditions. Out of the 23 active slip systems, 1 was basal (4 pct), 16 were prismatic (70 pct), 4 were pyramidal $\langle a \rangle$ (17 pct), and 2 were pyramidal $\langle c+a \rangle$ (9 pct). Prismatic slip was the primary slip system, which is similar to that observed for the tensile tests at 296 K and 728 K (23 °C and 455 °C). Twinning was not observed during the creep deformation.

IV. DISCUSSION

A. *The Effect of Texture on the Deformation System Activation*

To fully assess the deformation system activity as a function of testing condition, it is first necessary to understand the role of the underlying texture in biasing the activity of the different deformation systems. Since at least 69 pct of the active deformation systems were associated with Schmid factors greater than 0.4 in the tensile and tensile-creep specimens, it is insightful to examine the potential number of each deformation

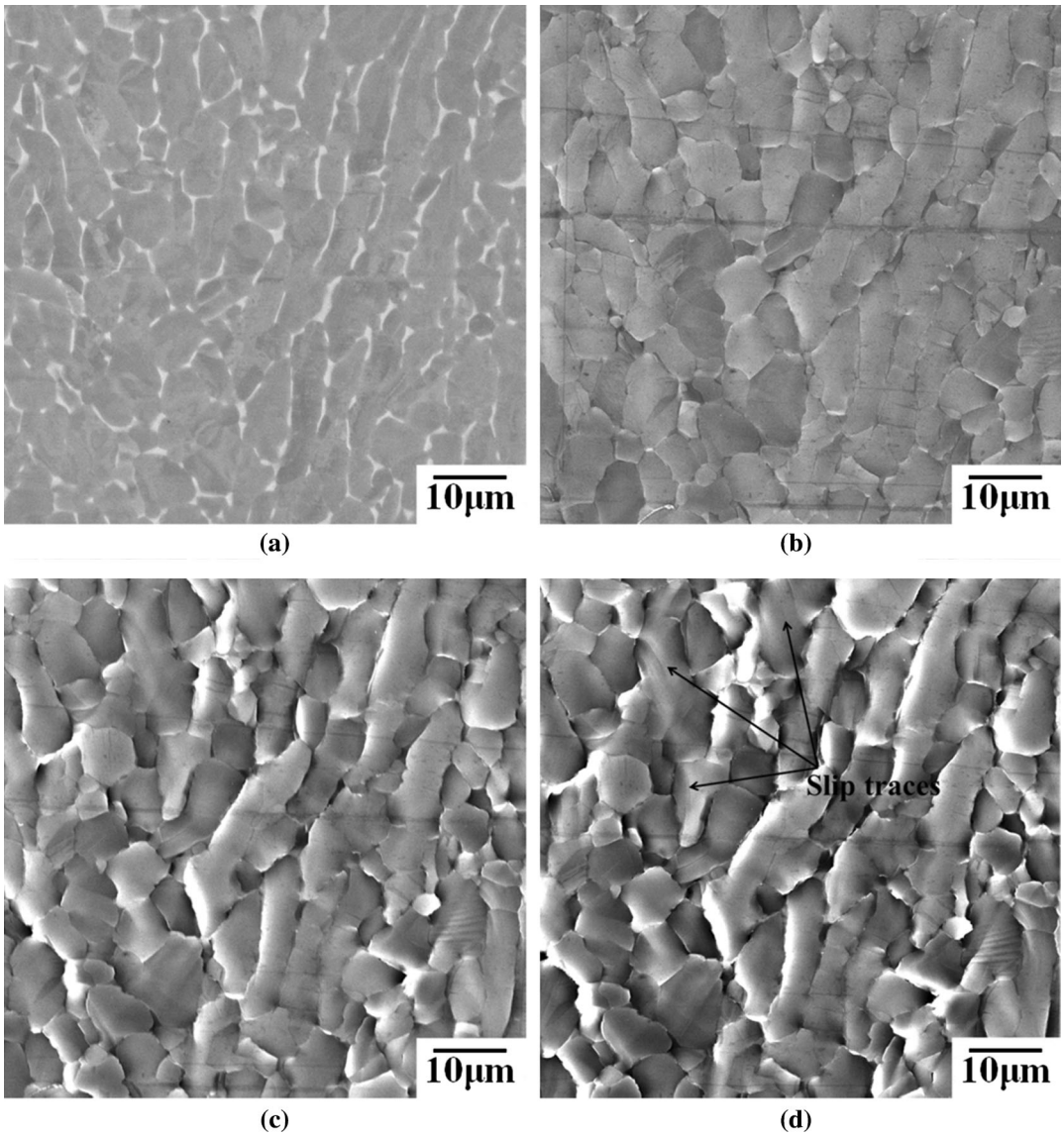

Fig. 14—SE SEM photomicrographs acquired during the 728 K (455 °C)-180 MPa creep experiment: (*a*) before loading; (*b*) ~1.4 pct strain; (*c*) ~6.6 pct strain; (*d*) ~11.7 pct strain. The loading direction was horizontal.

system type exhibiting Schmid factors greater than 0.4 (resulting from the texture) for each specimen and study how this affected the deformation system activity. For each grain, there are 3 basal, 3 prismatic, 6 pyramidal $\langle a \rangle$, 12 pyramidal $\langle c+a \rangle$, and 6 T1 twinning systems (other twinning systems were not observed and therefore they were ignored in this analysis). The number of each of these deformation types with Schmid factors greater than 0.4 were determined for each grain in each of the microstructural patches examined. Note that since dislocation slip is bidirectional, this determination was based on the absolute values of the Schmid factors of the 24 dislocation slip systems. Because twinning is unidirectional, only those systems with positive Schmid factors were considered. Table II summarizes the ratios of the number of the deformation systems exhibiting a Schmid factor of at least 0.4 for basal, prismatic, pyramidal $\langle a \rangle$, pyramidal $\langle c+a \rangle$, and T1 twins over the total number of deformation systems exhibiting a Schmid factor of at least 0.4 for all of the microstructural patches studied. For each row in Table II, the ratios add up to 1.

The ratios of the different deformation system types varied between plate 1 and plate 2, as shown in Table II, indicative of the significant texture differences. The prismatic slip ratios (0.16-0.18) for plate 1 were approximately twice the basal ratios (0.08), indicating that prismatic slip systems were on average more highly stressed in plate 1. However, in plate 2, the ratios for prismatic and basal slip were similar. The differences between the prismatic and basal Schmid factor ratios in plates 1 and 2 explain the much higher percentages of prismatic slip activity observed at the 296 K and 728 K (23 °C and 455 °C) tensile tests for plate 1 compared with plate 2 under the same testing conditions. Moreover, the ratios for basal slip in plate 1 (0.08) were lower than the ratios in plate 2 (0.10 to 0.13), consistent with the decreased basal activity observed in plate 1 [2 pct at

296 K (23 °C), 6 pct at 728 K (455 °C)] relative to plate 2 under the same testing conditions [8 pct at 296 K (23 °C), 14 pct at 728 K (455 °C)]. Likewise, the ratios for T1 twinning in plate 1 (0.05 to 0.07) were lower than in plate 2 (0.10 to 0.15), consistent with the reduced twin activity in plate 1 [10 pct at 296 K (23 °C), 4 pct at 728 K (455 °C)] compared with that in plate 2 tested under the same conditions [23 pct at 296 K (23 °C), 6 pct at 728 K (455 °C)]. Therefore, the differences of the deformation system activity observed in plate 1 and plate 2 likely resulted from the significant texture variations.

B. *Deformation Behavior in Comparison with CP Ti and Other Ti Alloys*

Prismatic slip was the dominant deformation system observed in this study, accounting for at least 48 pct of the observed deformation systems. Prismatic slip is also the preferred deformation mode in CP Ti.[1,12,14,33–35]

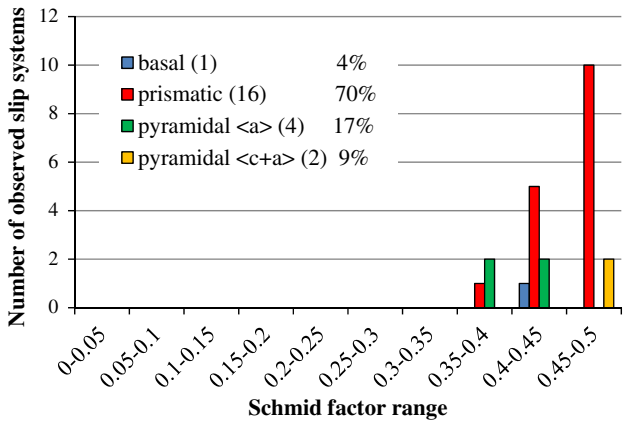

Fig. 15—Histogram of the number of observed slip systems *vs* the global Schmid factor range taken for the plate 1 tensile-creep tested at 728 K (455 °C)-180 MPa after ~11.7 pct strain.

For Ti-3Al-2.5V, basal slip accounted for no more than 14 pct of the total deformation modes observed for all the specimens tested. As noted above, the texture of plate 1 favored the activation of prismatic slip, while for plate 2 this was not the case and the texture did not bias the activation of prismatic slip over basal slip. For CP Ti, where basal and prismatic slip were equally stressed based on the texture, basal activity only accounted for 10 pct of the observed deformation systems for 296 K and 728 K (23 °C and 455 °C) tensile tests.[12] However, extensive basal activity has been observed in recent studies on Ti-5Al-2.5Sn,[12,18,36,37] Ti-6Al-4V,[27] and Ti-6Al.[38] It also has been shown that the basal slip activity increases with increasing Al content.[16] Thus, the relatively low activity of basal slip observed in this study may be attributed to the lower Al content in Ti-3Al-2.5V compared with Ti-5Al-2.5Sn, Ti-6Al-4V, and Ti-6Al.

The activation of the observed deformation systems in Ti-3Al-2.5V is pertinent to the high global Schmid factors. For Ti-3Al-2.5V, only a small portion of the activated deformation systems in the tension tests exhibited low global Schmid factors (2 to 8 pct of the activated deformation systems exhibited global Schmid factors below 0.3). This is unlike that observed for the tension tests performed on the Ti-5Al-2.5Sn alloy and the CP Ti, where more deformation systems were activated with low global Schmid factors (13 to 21 pct of the activated deformation systems exhibited global Schmid factors below 0.3).[12,18] This suggests that local stress concentrations are less likely to build up in the Ti-3Al-2.5V alloy, compared with the CP Ti and Ti-5Al-2.5Sn. This may be due to two reasons. First, Ti-3Al-2.5V exhibits a larger volume fraction (6.1 ± 1.1 pct β phase) of the soft grain boundary β phase than CP Ti and Ti-5Al-2.5Sn (<1 pct β phase) and the soft body center cubic β phase may act to mitigate stress concentrations during deformation. Indeed, observations have shown that the β phase, with a large number of slip systems, can readily accept slip transfer from the harder

Table II. Ratio of Slip Systems Exhibiting a Global Schmid Factor of at Least 0.4 for Basal, Prismatic, Pyramidal $\langle a \rangle$, Pyramidal $\langle c+a \rangle$, and T1 Twins Over the Total Number of Deformation Systems Exhibiting a Global Schmid Factor of at Least 0.4 for the Undeformed Microstructural Patch Characterized for Each Specimen

Specimen	Basal	Prismatic	Pyramidal $\langle a \rangle$	Pyramidal $\langle c+a \rangle$	T1 Twin
296 K (23 °C) tension, plate 1	0.08	0.18	0.24	0.45	0.05
728 K (455 °C) tension, plate 1	0.08	0.16	0.24	0.45	0.07
728 K (455 °C)-180 MPa creep, plate 1	0.09	0.17	0.24	0.45	0.05
296 K (23 °C) tension, plate 2	0.10	0.10	0.21	0.44	0.15
728 K (455 °C) tension, plate 2	0.13	0.10	0.22	0.45	0.10

Table III. Mean CRSS Ratios and the Corresponding 90 pct Confidence Interval of Basal, Prismatic, Pyramidal $\langle a \rangle$, Pyramidal $\langle c+a \rangle$, and T1 Twin Deformation Systems for Ti-3Al-2.5V at 296 K and 728 K (23 °C and 455 °C)

Specimen	$\frac{\text{Prismatic}}{\text{Basal}}$	$\frac{\text{Pyramidal } \langle a \rangle}{\text{Basal}}$	$\frac{\text{Pyramidal } \langle c+a \rangle}{\text{Basal}}$	$\frac{\text{T1 twin}}{\text{Basal}}$
296 K (23 °C) tension, plate 1	0.05 (0.01, 0.1)	1.1 (0.26, 2.8)	11.9 (0.81, 34.9)	0.23 (0.06, 0.52)
296 K (23 °C) tension, plate 2	0.16 (0.07, .25)	0.81 (0.31, 1.5)	5.7 (1.8, 12.5)	0.37 (0.14, 0.68)
728 K (455 °C) tension, plate 1	0.2 (0.07, 0.34)	1.2 (0.44, 2.3)	6.3 (1.8, 13.9)	2.2 (0.54, 5.6)
728 K (455 °C) tension, plate 2	0.33 (0.20, 0.50)	1.1 (0.62, 1.7)	12.3 (4.9, 25.2)	2.8 (14.6, 19.0)

α phase.[36] Second, compared with CP Ti (~115 μm α grain size) and Ti-5Al-2.5Sn (~45 μm α grain size), the Ti-3Al-2.5V in the current study exhibited a finer grain size (5.1 ± 0.8 μm), which is also effective in reducing stress concentrations.[39]

Twinning was an active deformation system during the 296 K and 728 K (23 °C and 455 °C) tension experiments. Generally, the addition of Al has been shown to suppress twinning in Ti alloys.[1,16] Therefore, it might be reasonable to expect less twinning activity in Ti-3Al-2.5V than in CP Ti. However, in our previous studies on CP Ti tensile deformed at 296 K (23 °C),[12] about 10 pct of the observed deformation systems were T1 twins, which is smaller than the 23 pct in the Ti-3Al-2.5V plate 2 tensile tested at 296 K (23 °C). However, a larger fraction of twins have been shown in CP Ti,[40–44] where the twin volume fraction has increased with increasing deformation for strains well above 10 pct. Most of these studies have been performed in RT compression or simple shear where the stages of deformation have been directly correlated to the twinning distribution and volume. Note that the ratio of twinning systems with Schmid factors greater than 0.4 out of the total number of deformation systems with Schmid factors greater than 0.4 was similar in the CP Ti tested at 296 K (23 °C) (0.18) and the Ti-3Al-2.5V plate 2 tested at 296 K (23 °C) (0.15). Zaefferer[1] concluded that lower oxygen concentration promotes twinning formation based on the observations that Ti with 0.1 wt pct (1000 ppm) oxygen was found to exhibit larger twinning activity than Ti with 0.2 wt pct (2000 ppm) oxygen. In the current study, the oxygen content was 0.085 wt pct for the Ti-3Al-2.5V 1 and 0.092 wt pct for the plate 2. These values are significantly lower than the 0.25 wt pct oxygen contained in the CP Ti in our previous study.[12] Thus, the relatively high twinning activity observed in the Ti-3Al-2.5V alloy in the present study may be partially explained by the low oxygen content.

C. *Creep*

Grain boundary sliding appeared to be more active than dislocation slip during creep. Using the calculated mechanistic creep parameters (*i.e.*, stress exponent and activation energy) of Ti-3Al-2.5V samples, Gollapudi *et al.*[24] concluded that grain boundary sliding was an active deformation mechanism in an intermediate stress regime ($0.6 \times 10^{-3}\ \sigma/E \sim 3 \times 10^{-3}\ \sigma$/E) in the temperature range of 723 K to 873 K (450 °C to 600 °C). The normalized stress value in Gollapudi's work was estimated considering the dependence of Young's Modulus on temperature (°C)[45]:

$$E(\text{GPa}) = 130.55 - 0.0777T.$$

Using this equation to normalize the creep stress, the test condition in the current work [$\sim 1.6 \times 10^{-3}\ \sigma/E$, 728 K (455 °C)] was similar to that in the Gollapudi *et al.*[24] study. The *in situ* observations of grain boundary ledge formation combined with limited slip traces in the current study provides evidence that GBS is an important deformation mechanism in the intermediate stress regime of Ti-3Al-2.5V.

The surface relief from the grain boundary sliding evident during creep was different than the surface relief observed during the tension experiments (compare Figures 5, 8, 10, 12, and 14). The surface relief observed during the tensile tests occurred for some clusters of grains and was more heterogeneous, while the grain boundary sliding in the creep test was observed for almost all the grains and occurred more homogenously. The reason for this could be that during the lower applied stress (*i.e.*, lower $\dot{\varepsilon}$) creep experiment (~250 hours), more diffusion was allowed to occur, resulting in more homogenous grain boundary sliding, compared with the approximately 2-hour tensile experiments.

D. *CRSS Ratios*

The CRSS values for the different deformation modes in Ti-3Al-2.5V have yet to be explored and by estimating the CRSS ratios of these deformation modes for this alloy, we can start to compare how microstructure and alloy composition affect the CRSS ratios of Ti alloys, which is not well known at this point. Thus, this study provides two new aspects to the literature on Ti-3Al-2.5V: a quantitative view of the distribution of the deformation modes and an estimation of the CRSS values using a methodology based on the distribution of the deformation modes. These two aspects are viewed by the authors as useful to the open literature.

A methodology for estimating the CRSS ratios for α-phase Ti based on slip-trace analysis of *in situ* deformed CP Ti and Ti-5Al-2.5Sn has been recently developed.[46] Following this methodology, the number of observations of each of the five deformation system types (*i.e.*, basal, prismatic, pyramidal $\langle a \rangle$, pyramidal $\langle c+a \rangle$, and T1 twinning) as a function of the global Schmid factor, which was binned with increments of 0.05, was recorded and placed into 10 Schmid factor bins for each of the five deformation system types. This distribution was called the experimentally observed deformation system-Schmid factor distribution. Next, for all the grains in a given microstructural patch of a given test, the number of potential deformation systems of a given deformation type and Schmid factor bin was calculated, regardless of whether the deformation system was activated or not. These data accounted for the texture and were binned in the same manner as for the experimentally observed deformation system-Schmid factor distribution, and they were referred as the potential deformation system-Schmid factor distribution. To reflect the fact that the activation of the deformation systems is a function of Schmid factors, a cubic function was used to modify the potential deformation system-Schmid factor distribution so that the number of deformation systems with small Schmid factors was strongly suppressed and the number of deformation systems with the highest Schmid factor bin (0.45 to 0.5) did not change. A least square optimization procedure was used to minimize the difference between the experimentally observed number

of deformation system distribution (from the slip trace analysis results) and the modified potential deformation system-Schmid factor distribution (accounting for the texture) in all of the grains from a given microstructure patch. The CRSS ratios of the different deformation systems were determined so that the texture-modified distribution could best match the experimental observations. The mean CRSS ratios among the different deformation systems and the associated confidence intervals were deduced by the bootstrapping statistical resampling technique described in Reference 46. Using this methodology, the mean CRSS ratios and the corresponding 90 pct confidence interval for the four different tensile specimens of Ti-3Al-2.5V are listed in Table III. The CRSS ratio values in the rest of the discussion refer to the mean CRSS ratios.

As shown in Table III, prismatic slip exhibited the lowest CRSS among all the deformation systems for all of the specimens examined, which is consistent with results from 296 K and 728 K (23 °C and 455 °C) tensile experiments on CP Ti.[12–15,18,46] The mean pyramidal $\langle a \rangle$-to-basal ratios were close to 1 at 296 K and 728 K (23 °C and 455 °C) for both plates, indicating that the CRSS of pyramidal $\langle a \rangle$ slip was compared with basal slip in the Ti-3Al-2.5V alloy. Pyramidal $\langle c+a \rangle$ slip exhibited the highest mean CRSS ratio among all the deformation modes for all the specimens evaluated, indicating that pyramidal $\langle c+a \rangle$ slip was the most difficult deformation mode to activate in the Ti-3Al-2.5V alloy. However, the relative activity of T1 twinning, compared with basal slip, changes as a function of temperature. At 296 K (23 °C) for both plate 1 and plate 2, T1 twinning exhibited a lower CRSS than basal slip (T1 twin/basal = 0.23 for specimen plate 1 and T1 twin/Basal = 0.37 for specimen plate 2). Increasing the temperature from 296 K to 728 K (23 °C to 455 °C) resulted in T1 twinning being less likely to activate than basal slip for both plates (T1 twin/basal = 2.2 for specimen plate 1 and T1 twin/basal = 2.8 for specimen plate 2) and basal slip became the second easiest deformation system to activate. This is consistent with the observations of Williams *et al.*,[16] where it was concluded that increasing temperature suppresses twinning and promotes basal slip. For Ti-3Al-2.5V, the CRSS ratios differed slightly from plate to plate. This may be due to the fact that the texture of plate 1 more strongly favored the activation of prismatic slip than the texture of plate 2. Nevertheless, the trends suggested by measurements from both plates show similar values and trends, and these CRSS ratios are consistent with the results from CP Ti and Ti-5Al-2.5Sn[46] as well as other alloys.[16]

V. CONCLUSIONS

Ti-3Al-2.5V was *in situ* tensile and tensile-creep tested at 296K (23 °C) and 728K (455 °C). An EBSD-based slip-trace analysis showed that prismatic slip was the dominant slip mode in all the specimens tested. Specimens from plate 1, which contained a texture favoring prismatic slip, exhibited a significantly greater fraction of prismatic slip than specimens from 2, which had a texture less favorable for prismatic slip. Twinning was an active deformation mode in both the 296 K and 728 K (23 °C and 455 °C) tension experiments. Compared with plate 1, there were higher fractions of T1 twinning activity in plate 2, which was more favorably orientated for activating T1 twinning systems, at both 296 K and 728 K (23 °C and 455 °C) tension. More dislocation slip and surface topography relief were observed during the 728 K (455 °C) tension test compared with the 296 K (23 °C) tension tests. During creep, grain boundary sliding appeared to be more active than dislocation slip. From the CRSS ratio analysis, it was determined that prismatic slip was easier to activate than basal slip and twinning at both 296 K and 728 K (23 °C and 455 °C), and twinning was easier to activate than basal slip at 296 K (23 °C), but less likely to activate than basal slip at 728 K (455 °C).

ACKNOWLEDGMENTS

This research was supported by the US Department of Energy, Office of Basic Energy Science through Grant No. DE-FG02-09ER46637. The authors are grateful to Mr. A. Chakkedath and Dr. J. Seal of Michigan State University for their intellectual discussions and assistance with sample preparation. The authors are grateful to T. Van Daam of Pratt & Whitney Rocketdyne for providing the materials used in this study. The authors are also grateful to Dr. D. Mason of Albion College for his assistance in the development of the CRSS-ratio determination methodology.

REFERENCES

1. S. Zaefferer: *Mater. Sci. Eng. A*, 2003, vol. 344, pp. 20–30.
2. P.S. Follansbee and G.T. Gray: *Metall. Trans. A*, 1989, vol. 20A, pp. 863–74.
3. P.D. Littlewood, T.B. Britton, and A.J. Wilkinson: *Acta Mater.*, 2011, vol. 59, pp. 6489–6500.
4. D.G.L. Praksah, R. Ding, R.J. Moat, I. Jones, P.J. Withers, J.Q. da Fonseca, and M. Preuss: *Mater. Sci. Eng. A*, 2010, vol. 527A, pp. 5734–44.
5. F. Bridier, P. Villechaise, and J. Mendez: *Acta Mater.*, 2008, vol. 56, pp. 3951–62.
6. T.R. Bieler and S.L. Semiatin: *Int. J. Plast.*, 2002, vol. 18, pp. 1165–89.
7. A.L. Pilchak, R.E.A. Williams, and J.C. Williams: *Metall. Mater. Trans. A*, 2010, vol. 41A, pp. 106–24.
8. J.S. Kim, Y.W. Chang, and C.S. Lee: *Metall. Mater. Trans. A*, 1998, vol. 29A, pp. 217–26.
9. M.J. Donachie: *Titanium: A Technical Guide*, 2nd ed., ASM International, Materials Park, OH, 1988.
10. R. Boyer, G. Welsch, and E.W. Collings, eds.: *Materials Properties Handbook: Titanium Alloys*, ASM International, Materials Park, OH, 1994.
11. S. Nemat-Nasser, W.G. Guo, and J.Y. Cheng: *Acta Mater.*, 1999, vol. 47, pp. 3705–20.
12. H. Li, D. Mason, Y. Yang, T.R. Bieler, M.A. Crimp, and C.J. Boehlert: *Philos. Mag.*, 2013, vol. 93, pp. 2875–95.
13. M.H. Yoo, J.R. Morris, K.M. Ho, and S.R. Agnew: *Metall. Trans. A*, 2002, vol. 33A, pp. 813–22.
14. J. Gong and A.J. Wilkinson: *Acta Mater.*, 2009, vol. 57, pp. 5693–05.

15. Y. Yang, L. Wang, T.R. Bieler, P. Eisenlohr, and M.A. Crimp: *Metall. Mater. Trans. A*, 2011, vol. 42A, pp. 636–44.
16. J.C. Williams, R.G. Baggerly, and N.E. Paton: *Metall. Mater. Trans. A*, 2002, vol. 33A, pp. 837–50.
17. L. Xiao: *Mater. Sci. Eng. A*, 2005, vol. 394, pp. 168–75.
18. H. Li, C.J. Boehlert, T.R. Bieler, and M.A. Crimp: *Philos. Mag.*, 2012, vol. 92, pp. 2923–46.
19. F. Coghe, W. Tirry, L. Rabet, D. Schryvers, and P. Van Houtte: *Mater. Sci. Eng. A*, 2012, vol. 537, pp. 1–10.
20. W. Tirry, F. Coghe, S. Bouvier, M. Gasperini, L. Rabet, and D. Schryvers: *Mater. Sci. Eng. A*, 2010, vol. 527, pp. 4136–45.
21. R. Boyer, G. Welsch, and E.W. Collings: *Materials Properties Handbook: Titanium Alloys*, ASM International, Metals Park, OH, 1994, p. 263.
22. A. Kumar, M. Sapp, J. Vincelli, and M.C. Gupta: *J. Mater. Process. Technol.*, 2010, vol. 210, pp. 64–71.
23. S. Gollapudi, V. Bhosle, I. Charit, and K.L. Murty: *Philos. Mag.*, 2008, vol. 88, pp. 1357–67.
24. S. Gollapudi, I. Charit, and K.L. Murty: *Acta Mater.*, 2008, vol. 56, pp. 2406–19.
25. V. Venkatesan, D.S. Sarma, and K.L. Murty: *J. Mater. Sci. Lett.*, 1991, vol. 10, pp. 984–86.
26. C.J. Boehlert, C.J. Cowen, S. Tamirisakandala, D.J. McEldowney, and D.B. Miracle: *Scripta Mater.*, 2006, vol. 55, pp. 465–68.
27. F. Bridier, P. Villechaise, and J Mendez: *Acta Mater.*, 2005, vol. 53, pp. 555–67.
28. C.J. Boehlert, Z Chen, I. Gutiérrez-Urrutia, J. Llorcab, and M.T. Pérez-Prado: *Acta Mater.*, 2012, vol. 60, pp. 1889–1904.
29. B.S. Fromm, B.L. Adams, S. Ahmadi, and M. Knezevic: *Acta Mater.*, 2009, vol. 57, pp. 2339–48.
30. M.G. Glavicic, P.A. Kobryn, T.R. Bieler, and S.L. Seminatin: *Mater. Sci. Eng. A*, 2003, vol. 351, pp. 258–64.
31. M.G. Glavicic, P.A. Kobryn, T.R. Bieler, and S.L. Seminatin: *Mater. Sci. Eng. A*, 2003, vol. 346, pp. 50–59.
32. J.W. Christian and S. Mahajan: *Prog. Mater. Sci.*, 1995, vol. 39, pp. 1–157.
33. L. Wang, R.I. Barabash, Y. Yang, T.R. Bieler, M.A. Crimp, P. Eisenlohr, W. Liu, and G.E. Ice: *Metall. Mater. Trans. A*, 2011, vol. 42A, pp. 626–35.
34. Z. Zeng, Y. Zhang, and S. Jonsson: *Mater. Sci. Eng. A*, 2009, vols. 513–514, pp. 83–90.
35. S. Farenc, D. Caillard, and A. Couret: *Acta Metall. Mater.*, 1993, vol. 41, pp. 2701–09.
36. J.R. Seal, M.A. Crimp, T.R. Bieler, and C.J. Boehlert: *Mater. Sci. Eng. A*, 2012, vol. 552, pp. 61–68.
37. A.L. Pilchak and J.C. Williams: *Metall. Mater. Trans. A*, 2010, vol. 41A, pp. 22–25.
38. T. Neeraj, D.H. Hou, G.S. Daehn, and M.J. Mills: *Acta Mater.*, 2000, vol. 48, pp. 1225–38.
39. A. Lasalmonie and J.L. Strudel: *J. Mater. Sci.*, 1986, vol. 21, pp. 1837–52.
40. M. Knezevic, R.A. Lebensohn, O. Cazacu, B. Revil-Baudard, G. Proust, S.C. Vogel, and M.E. Nixon: *Mater. Sci. Eng. A*, 2013, vol. 564, pp. 116–26.
41. W Tirry, S Bouvier, N Benmhenni, W Hammami, AM Habraken, F Coghe, D Schryvers, and L Rabet: *Mater. Charact.*, 2012, vol. 72, pp. 24–36.
42. S. Bouvier, N. Benmhenni, W. Tirry, F. Gregory, M.E. Nixon, O. Cazacu, and L. Rabet: *Mater. Sci. Eng. A*, 2012, vol. 535, pp. 12–21.
43. W. Tirry, M. Nixon, O. Cazacu, F. Coghe, and L. Rabet: *Scripta Mater.*, 2011, vol. 64, pp. 840–43.
44. A.A. Salem, S.R. Kalidindi, and R.D. Doherty: *Acta Mater.*, 2003, vol. 51, pp. 4225–37.
45. E.S. Fisher and C.J. Renken: *Phys. Rev.*, 1964, vol. 135, pp. A482–94.
46. H. Li, D.E. Mason, T.R. Bieler, C.J. Boehlert, and M.A. Crimp: *Acta Mater.*, 2013, vol. 61, pp. 7555–67.